Postprint of: Żak A., Krawczuk M., Redlarski G., Doliński Ł., Koziel S., A three-dimensional periodic beam for vibroacoustic isolation purposes, Mechanical Systems and Signal Processing, Vol. 130 (2019), pp. 524-544, DOI: 10.1016/j.ymssp.2019.05.033

A three-dimensional periodic beam for vibroacoustic isolation purposes

A. Żak[a,*], M. Krawczuk[a], G. Redlarski[a], Ł. Doliński[a], S. Koziel[b]

[a] *Gdansk University of Technology, Faculty of Electrical and Control Engineering, Narutowicza 11/12, 80-234 Gdansk, Poland*
[b] *Reykjavik University, School of Science and Engineering, Menntavegur 1, 101 Reykjavik, Iceland*

Abstract

This paper presents results of investigations on a three-dimensional (3-D) isotropic periodic beam. The beam can represent a vibroacoustic isolator of optimised dynamic characteristics in the case of its longitudinal, flexural and torsional behaviour. The optimisation process concerned both the widths as well as the positions of particular frequency band gaps that are present in the frequency spectrum of the beam. Since the dynamic behaviour of the beam is directly related to its geometry, through an optimisation process of the beam geometry, desired dynamic characteristics of the beam were successfully obtained. For the purpose of the optimisation process a new numerical model of the beam, based on the spectral finite element method in the time domain (TD-SFEM), was developed by the authors. This model enabled the authors to investigate the beam behaviour not only in a wide frequency spectrum, but also ensured a high accuracy of the model predictions. The accuracy of this modelling approach was checked against well-known analytical formulas. However, in the case of the optimised geometry of the beam for the verification of the correctness of the modelling approach a commercial finite element method (FEM) package was used. Finally, based on the results of numerical predictions and optimised geometry of the beam a sample for experimental verification was prepared. Experimental measurements were carried out by the authors by the application of one-dimensional (1-D) laser Doppler scanning vibrometry (LDSV). The results of experimental measurements obtained by the authors confirmed the correctness of the numerical predictions, showing a high degree of correspondence.

Keywords: periodic beam; spectral finite element method; elastic wave propagation; frequency band gaps

1. Introduction

For many decades now periodic structures have been remaining the area of great scientific interest [1–10]. During that time unusual properties of periodic structures have been investigated using various methods and techniques. They have been studied not only analytically by such methods as the plane expansion method (PEM) [1–5] or the transfer matrix method (TMM) [6, 7], but also experimentally [1, 3–7] or numerically thanks to the application of sophisticated computational tools based on the classical finite element method (FEM) [8–11], to mention only the most common ones.

Periodic structures, in a similar way to periodic metamaterials [12–14], exhibit the same unusual dynamic behaviour thanks to the periodicity of their structures [15] that is attributed to their cellular arrangement. The source of this periodicity may come from periodic variations of material properties within their cells (density or elastic modulus) and/or variations in the cell geometry (cross-section or presence of certain geometrical features). It should be noted that in the case of periodic structures, periodic variations of their

*Corresponding author
Email addresses: arkadiusz.zak@pg.edu.pl (A. Żak), marek.krawczuk@pg.edu.pl (M. Krawczuk), grzegorz.redlarski@pg.edu.pl (G. Redlarski), lukasz.dolinski@pg.edu.pl (Ł. Doliński), koziel@ru.is (S. Koziel)

structural properties within the cells in macro-scale influences their observable dynamic behaviour at the same scale. The periodicity of periodic structures manifests itself in the presence of so-called frequency band gaps in their frequency spectra, which indicate frequency regions within which no energy can be transmitted through these structures [6–11]. This feature may lead to many interesting, potential applications of periodic structures, mainly in vibroacoustics.

One such application for periodic structures is vibroacoustic isolation or filtering of propagating vibroacoustic signals in given frequency bands. It should be noted that in order to achieve desired isolation or filtering properties periodic structures must be precisely designed. This process usually includes certain optimisation procedures [16] that lead to the predefined widths as well as the positions of particular frequency band gaps. In this manner various types of propagating vibroacoustic signals (longitudinal, flexural or torsional) within periodic structures can be selectively isolated or filtered out depending on the needs of particular applications.

It should be noted that analytical investigations of periodic structures have usually been limited one-dimensional (1-D) or two-dimensional (2-D) structures of simple geometries and boundary conditions. Contrary to this the FEM seems free of these limitations and appears as a tool capable to tackle problems of complex three-dimensional (3-D) geometries, arbitrary boundary conditions as well as material properties.

In the current work a 3-D isotropic, periodic beam is investigated by the authors for vibroacoustic isolation purposes. The 3-D nature of the beam geometry results in the propagation of three types of vibroacoustic signals within the beam, which are: longitudinal, flexural and torsional elastic waves. Since the dynamic behaviour of the beam is directly related to its geometry, through an optimisation process of the beam geometry, desired dynamic characteristics of the beam were successfully obtained. For this reason dynamic characteristics for each type of vibroacoustic signal of the beam were considered and investigated by the authors. Based on these characteristics both the widths and the positions of particular frequency band gaps, that are present in the frequency spectrum of the beam, were precisely tailored to certain predefined, desired requirements.

For the purpose of the optimisation process a new numerical model of the beam, based on the spectral finite element method in the time domain (TD-SFEM), was developed by the authors providing smooth and continuous variation of the beam geometry. This model enabled the authors to investigate the beam behaviour not only in a wide frequency spectrum, but also ensured a high accuracy of the model predictions. The accuracy of this modelling approach was also checked against well-known analytical formulas. However, in the case of the optimised geometry of the beam used to verify the correctness of the modelling approach a commercial FEM package was also used. Finally, based on the results of numerical predictions and optimised geometry of the beam a sample for experimental verification was prepared. Experimental measurements were carried out by the authors by the application of 1-D laser Doppler scanning vibrometry (LDSV). The results of experimental measurements obtained by the authors confirmed the correctness of the numerical predictions, showing a high degree of correspondence.

The results presented in this paper also indicate the capabilities offered by numerical modelling and optimisation methods that can be successfully employed in order to design periodic structures of predefined dynamic properties, i.e. the widths and the positions of frequency band gaps in their vibration spectra.

2. Problem description

All results presented in this work concern a 3-D isotropic, periodic and axisymmetrical beam, which is schematically presented in Fig. 1. It was assumed that the periodic beam was divided into $N = 40$ identical cells of a continuously varying radius $R(x)$ in the range between $R_1 = 5$ mm and $R_2 = 50$ mm, where x denotes a coordinate measured along the length of the beam. The total length of the beam was $L = 1000$ mm, therefore the length of a particular cell was $L/N = 25$ mm. Additionally, it was assumed that each cell was subdivided into $s = 5$ segments equal in length.

The variation of the radius $R(x)$ within the i-th segment is described by a radius function $r_i(\xi)$, which is defined as a smooth polynomial $p(\xi)$ of degree $n = 5$, defined as follows:

$$p(\xi) = r_i(\xi) = r_i(1 - 10\xi^3 + 15\xi^4 - 6\xi^5) + r_{i+1}(10\xi^3 - 15\xi^4 + 6\xi^5), \quad i = 1, \ldots, s, \quad \xi \in <0, 1> \tag{1}$$

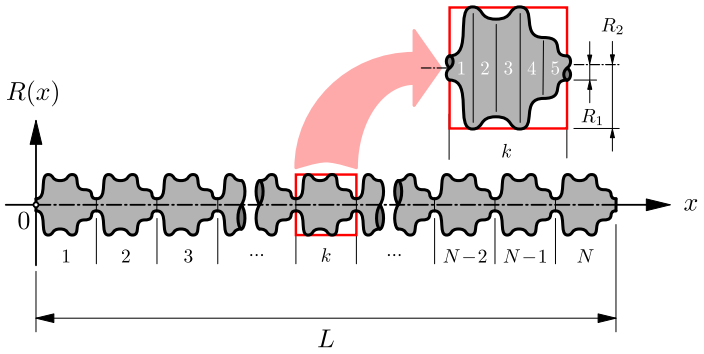

Figure 1: The concept of geometry of a 3-D isotropic, periodic and axisymmetrical beam.

where now ξ is a non-dimensional coordinate measured along each i-th segment. Certain boundary conditions at the the beginning ($\xi = 0$) and the end ($\xi = 1$) of the i-th segment were used in order to define the polynomial $p(\xi)$. These included polynomial values $p(0) = r_i$ and $p(1) = r_{i+1}$, as well as the values of its two derivatives $p'(0) = p''(0) = p'(1) = p''(1) = 0$, respectively. The variation of the polynomial $p(\xi)$ and its derivatives $p'(\xi)$, $p''(\xi)$ and $p'''(\xi)$ within the i-th segment are presented in Fig. 2. They were normalised with respect to their maxima for the values of $r_i = 1$ mm and $r_{i+1} = 4$ mm.

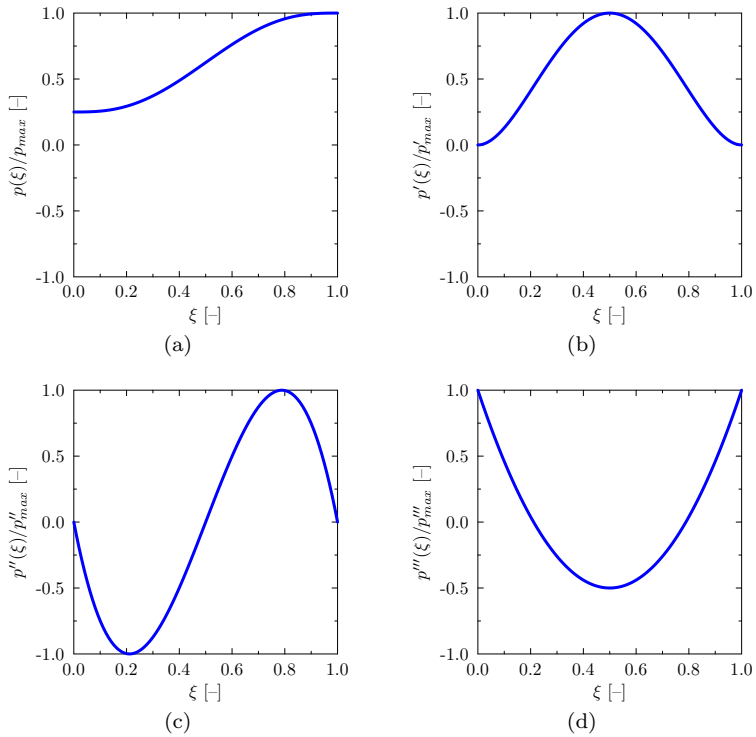

Figure 2: Typical variation of the polynomial $p(\xi)$ (a) and its derivatives $p'(\xi)$ (b), $p''(\xi)$ (c) as well as $p'''(\xi)$ (d) within the i-th segment of a cell, for the values of $r_i = 1$ mm and $r_{i+1} = 4$ mm.

It can be clearly seen from Fig. 2 that the polynomial $p(\xi)$ is a smooth polynomial up to its 3-rd derivative, and it remains continuous between each segment of the cell, as $p'(0) = p'(1)$, $p''(0) = p''(1)$ and $p'''(0) = p'''(1)$. For this reason the variation of the radius $R(x)$ is also smooth, not only along each cell, but also along the whole beam length. As a consequence of the beam periodicity it can be found that $r_1 = r_s$.

It was assumed that the beam was made out of an aluminium alloy of the following material properties:

Young's modulus $E = 67.5$ MPa, Poisson's ratio $\nu = 0.33$, mass density $\rho = 2700$ kg/m^3.

A very important aspect of the current consideration is the type of boundary conditions of the beam, which the authors assumed as free rather than periodic. This means than both ends of the beam remained free and a certain influence of the finite length of the beam could be observed during the current analysis. It can be found in the available literature [17] that this influence may be practically neglected for the total number of cells within a structure $N \gg 1$. In practice the number of cells N equal to 100 turns out to be sufficient. For smaller numbers of cells N this influence may be observable. However, in the case of the beam under investigation, consisting of 40 cells, and the selected type of boundary conditions, this influence remained unnoticed.

3. Numerical model

Based on the above description of a 3-D isotropic, periodic and axisymmetrical beam a suitable numerical model was built by the authors. This model enabled the authors to study the dynamic behaviour of the beam in terms of its natural vibration responses in a wide range of natural frequencies. Subsequently the numerical model developed by the authors was used as a base for a certain optimisation procedure, through which desired dynamic characteristics of the beam were successfully obtained.

3.1. Description of the spectral finite elements

As a modelling technique the spectral finite element method in the time-domain (TD-SFEM) was selected by the authors [18]. It was assumed that the beam was divided into a number of spectral finite elements (SFEs). Three types of beam natural vibration responses were analysed, these being: longitudinal, flexural and torsional vibrations. Due to the axial symmetry of the beam (no geometrical coupling) these three types of natural vibrations could be analysed independently [19].

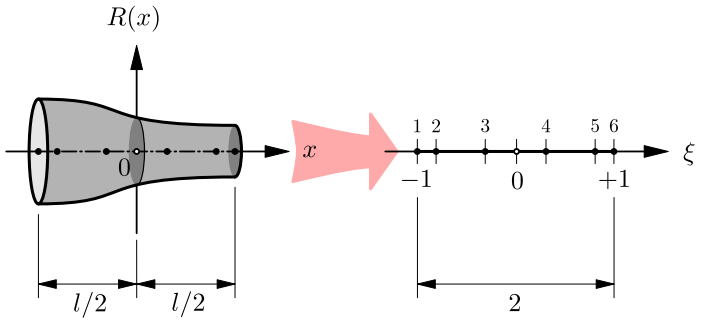

Figure 3: A 6-node spectral finite element used for modelling natural vibration responses of a 3-D isotropic, periodic and axisymmetrical beam, based on Chebyshev node distribution, in the global x (left) and local-normalised ξ (right) coordinate systems.

Independently of the type of beam vibrational responses, 6-node SFEs based on Chebyshev node distribution were used [20]. The coordinates of their nodes were defined in the local coordinate system ξ of the element as the roots of the following polynomial expression, as presented in Fig. 3:

$$T_n^c(\xi) \equiv (1-\xi^2)U_{n-2}(\xi) = 0, \quad |\xi| \leq 1 \tag{2}$$

where $U_{n-2}(\xi)$ is a Chebyshev polynomial of the second kind and degree $n-2$, while $T_n^c(\xi)$ is a complete Chebyshev polynomial of degree n. In this case the coordinates of the element nodes ξ_i can be calculated from the relation:

$$\xi_j = -\cos\beta_j, \quad \beta_j = \frac{\pi(j-1)}{n}, \quad j = 1, \ldots, n+1 \tag{3}$$

leading to the following values:

$$\begin{cases} \xi_1 = -\xi_6 = -1.0 \\ \xi_2 = -\xi_5 = \frac{1}{4}(-1-\sqrt{5}) \cong -0.80901699 \\ \xi_3 = -\xi_4 = \frac{1}{4}(+1-\sqrt{5}) \cong -0.30901699 \end{cases} \tag{4}$$

On the specified set of nodes ξ_j, in the local-normalised coordinate system of the element ξ, elemental shape functions can be built [18]. An interpolation function $f(\xi)$ supported on the element nodes ξ_j can be defined in the following way:

$$f(x) = \sum_{j=1}^{n+1} N_j(\xi) f_j, \quad |x| \leq \frac{l}{2}, \quad \xi = \frac{2x}{l} \tag{5}$$

where now $N_j(\xi)$ denotes 1-D shape functions of the element, f_j are unknown nodal values, while l is the length of a single SFE.

In the current case 1-D shape functions of the element $N_j(\xi)$ of degree $n = 5$, equal to the degree of the polynomial $p(\xi)$ describing the variation of the radius function $r_i(\xi)$ within each segment of the beam, were chosen. They are presented in Fig. 4. Since the geometry of the beam is described by polynomials of the same degree as elemental independent variables by the 1-D shape functions, the current definition of SFEs used by the authors reflects the definition of isoparametric SFEs.

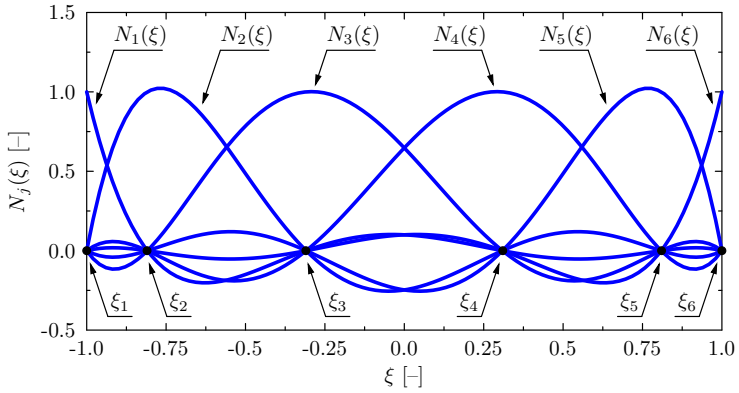

Figure 4: 1-D shape functions $N_j(\xi)$ of degree $n = 5$ of the element based on Chebyshev node distribution, in the local-normalised coordinate system ξ.

3.2. Displacement and strain fields

Due to the axial symmetry of the beam under consideration its natural vibration responses can be investigated as uncoupled. As a result of this symmetry also the displacement fields associated with longitudinal, flexural and torsional behaviour of the beam can be defined independently [19]. Such an approach enables the authors to simplify significantly the requirements of the current analysis without any loss of quality of simulation results [18].

It was assumed by the authors that the displacement fields under consideration were based on the McLaurin expansions up to order 5 of the unknown functions of displacement components: axial u_x, radial u_r and tangential u_θ, in the cylindrical coordinate system $xr\theta$ rather than in the Cartesian coordinate system xyz. They were assumed to be dependent on spatial coordinates x, y and z as well as time t. It should be noted here that depending on the type of the displacement field certain elements of these expansions may vanish, as also does their dependence on certain spatial coordinates. Typical distributions of axial u_x, radial u_r and tangential u_θ displacement components within the cross-section of the beam under investigation, in the case of longitudinal, flexural and torsional behaviour, are shown in Fig. 5.

Taking into account the points mentioned above the three displacement fields can be presented in the following manner as [21, 22]:

■ 6-mode theory of *longitudinal behaviour*[23]:

$$\begin{cases} u_x(x,r,t) = \phi_0(x,t) + r^2\phi_2(x,t) + r^4\phi_4(x,t) \\ u_r(x,r,t) = r\psi_1(x,t) + r^3\psi_3(x,t) + r^5\psi_5(x,t) \\ u_\theta(x,r,t) = 0 \end{cases} \tag{6}$$

where the displacement components u_x, u_r and u_θ are independent of the coordinate θ due to the axial symmetry of the beam with respect to the x-axis. As a result of this the displacement component u_θ must also vanish.

■ 8-mode theory of *flexural behaviour* [24]:

$$\begin{cases} u_x(x,r,\theta,t) = [r\phi_1(x,t) + r^3\phi_3(x,t) + r^5\phi_5(x,t)]\sin\theta \\ u_r(x,r,\theta,t) = [\psi_0(x,t) + r^2\psi_2(x,t) + r^4\psi_4(x,t)]\sin\theta \\ u_\theta(x,r,\theta,t) = [\psi_0(x,t) + r^2\vartheta_2(x,t) + r^4\vartheta_4(x,t)]\cos\theta \end{cases} \tag{7}$$

where the form of the displacement field corresponds to bending in the xy-plane, while the factors $\sin\theta$ and $\cos\theta$ associate the current displacement field with the fundamental branch of solutions [21, 22], this branch being the most important in practical applications.

■ 3-mode theory of *torsional behaviour*:

$$\begin{cases} u_x(x,r,t) = 0 \\ u_r(x,r,t) = 0 \\ u_\theta(x,r,t) = r\vartheta_1(x,t) + r^3\vartheta_3(x,t) + r^5\vartheta_5(x,t) \end{cases} \tag{8}$$

where the displacement components u_x, u_r and u_θ are independent of the coordinates x and y due to the purely torsional nature of the displacement field. As a result of this the displacement components u_x and u_r must also vanish.

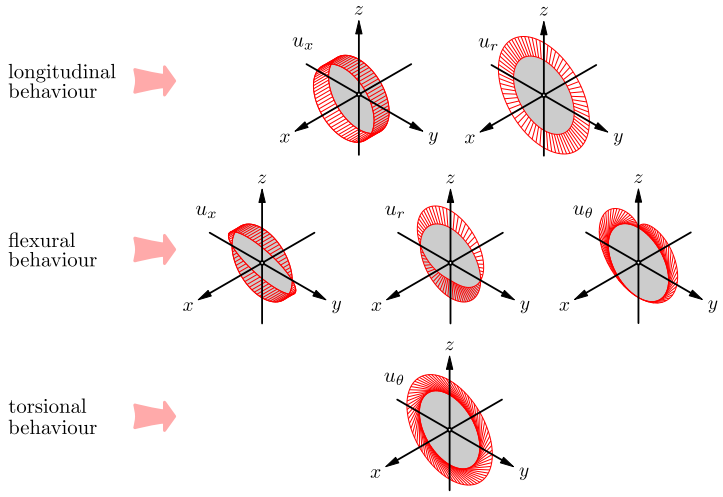

Figure 5: Distribution of axial u_x, radial u_r and tangential u_θ displacement components within the circular cross-section of a beam element in the case of longitudinal, flexural and torsional behaviour.

Assuming small strains within the beam the corresponding strain fields can be determined in the cylindrical coordinate system $xr\theta$, based on the well-known formulae [19], as:

■ 6-mode theory of *longitudinal behaviour*[23]:

$$\begin{cases} \epsilon_{xx} = \dfrac{\partial u_x}{\partial x} = \phi_0'(x,t) + r^2\phi_2'(x,t) + r^4\phi_4'(x,t) \\ \epsilon_{rr} = \dfrac{\partial u_r}{\partial r} = \psi_1(x,t) + 3r^2\psi_3(x,t) + 5r^4\psi_5(x,t) \\ \epsilon_{\theta\theta} = \dfrac{u_r}{r} = \psi_1(x) + r^2\psi_3(x) + r^4\psi_5(x) \\ \gamma_{xr} = \dfrac{\partial u_x}{\partial r} + \dfrac{\partial u_r}{\partial x} = 2r\phi_2(x,t) + 4r^3\phi_4(x,t) + r\psi_1'(x,t) + r^3\psi_3'(x,t) + r^5\psi_5'(x,t) \end{cases} \tag{9}$$

where the strain components $\gamma_{r\theta}$ and $\gamma_{\theta x}$ vanish due to the axial symmetry with respect to the x-axis.

■ 8-mode theory of *flexural behaviour* [24]:

$$\begin{cases} \epsilon_{xx} = \dfrac{\partial u_x}{\partial x} = [r\phi_1(x,t) + r^3\phi_3(x,t) + r^5\phi_5(x,t)]\sin\theta \\ \epsilon_{rr} = \dfrac{\partial u_r}{\partial r} = [2r\psi_2(x,t) + 4r^3\psi_4(x,t)]\sin\theta \\ \epsilon_{\theta\theta} = \dfrac{u_r}{r} + \dfrac{1}{r}\dfrac{u_\theta}{\partial\theta} = [r\psi_2(x,t) + r^3\psi_4(x,t) - r\vartheta_2(x,t) - r^3\vartheta_4(x,t)]\sin\theta \\ \gamma_{xr} = \dfrac{\partial u_x}{\partial r} + \dfrac{\partial u_r}{\partial x} = [\phi_1(x,t) + 3r^3\phi_3(x,t) + 5r^4\phi_5(x,t) + \psi_0'(x,t) + r^3\psi_2'(x,t) + r^4\psi_4'(x,t)]\sin\theta \\ \gamma_{r\theta} = \dfrac{1}{r}\dfrac{\partial u_r}{\partial\theta} + \dfrac{\partial u_\theta}{\partial r} - \dfrac{u_\theta}{r} = [r\psi_2(x,t) + r^3\psi_4(x,t) + r\vartheta_2(x,t) + r^3\vartheta_4(x,t)]\cos\theta \\ \gamma_{\theta x} = \dfrac{\partial u_\theta}{\partial x} + \dfrac{1}{r}\dfrac{\partial u_x}{\partial\theta} = [\phi_1(x,t) + r^2\phi_3(x,t) + r^4\phi_5(x,t) + \psi_0'(x,t) + r^2\vartheta_2'(x,t) + r^4\vartheta_4'(x,t)]\cos\theta \end{cases} \tag{10}$$

■ 3-mode theory of *torsional behaviour*:

$$\begin{cases} \gamma_{r\theta} = \dfrac{\partial u_\theta}{\partial r} - \dfrac{u_\theta}{r} = 2r^2\vartheta_3(x,t) + 4r^4\vartheta_5(x,t) \\ \gamma_{\theta x} = \dfrac{\partial u_\theta}{\partial x} = r\vartheta_1'(x,t) + r^3\vartheta_3'(x,t) + r^5\vartheta_5'(x,t) \end{cases} \tag{11}$$

where the remaining strain components vanish due to the purely torsional nature of the displacement field.

3.3. Dispersion curves

Dispersion curves carry very important information about the frequency behaviour of each theory considered by the authors. But most of all they help to determine the range of applications of each theory and agreement with known analytical solutions. In the case of the displacement fields presented in the previous section, associated with the theories of longitudinal, flexural and torsional behaviours of the beam, the dispersion curves can be evaluated by the use of Hamilton's principle [25]. Based on given displacement fields the virtual work W, related to the deformation and motion of the beam, may be expressed in terms of the strain energy U, the kinetic energy T as well as the work of some external forces W_e as:

$$\int_{t_1}^{t_2} \delta W dt = \int_{t_1}^{t_2} (\delta W_e + \delta T - \delta U) dt = 0 \tag{12}$$

with an additional assumption made only for the purpose of the current considerations, of a constant cross-section of the beam, defined by the radius a.

Application of Hamilton's principle at this point leads to a set of equations of motion that can be derived for each displacement field component, as presented in [23, 24].

Next, by assuming that only harmonic waves can propagate within the beam the equations of motion can be transformed from a set of partial differential equations, defined in the time domain for each displacement

component, to a set of linear homogeneous equations defined in the frequency domain, but for the amplitudes of each displacement component. This system can then be solved only when its determinant vanishes, which leads directly to a characteristic polynomial equation. The roots of the characteristic polynomial define dispersion relations between the wave number k and the angular frequency ω of particular modes of these waves.

The dispersion curves for each theory discussed in this paper were obtained by the application of *Mathematica* package [26], for all required analytical manipulations, while for necessary numerical calculations related to the evaluation of the dispersion curves the authors employed *MATLAB* package [27].

The above mentioned procedure is discussed below in more detail for the case of the 3-mode theory of torsional behaviour of the beam from the previous section of the paper given by Eqs. (8). The kinetic energy T and the strain energy U of the beam can be evaluated from:

$$\begin{cases} T = \dfrac{1}{2}\displaystyle\int_V \tilde{T} dV = \dfrac{1}{2}\int_V \rho\, \dot{u}_\theta^2 dV \\ U = \dfrac{1}{2}\displaystyle\int_V \tilde{U} dV = \dfrac{1}{2}\int_V (\gamma_{r\theta}\tau_{r\theta} + \gamma_{\theta x}\tau_{\theta x}) dV \end{cases} \tag{13}$$

where ρ is the beam material density and V its volume:

$$\begin{cases} \tilde{T} = \rho[a\dot{\vartheta}_1(x,t) + a^3\dot{\vartheta}_3(x,t) + a^5\dot{\vartheta}_5(x,t)]^2 \\ \tilde{U} = \mu a^2[\vartheta_1'(x,t) + a^2\vartheta_3'(x,t) + a^4\vartheta_5'(x,t)]^2 + 4\mu a^4[\vartheta_3'(x,t) + 2a^2\vartheta_5'(x,t)]^2 \end{cases} \tag{14}$$

where the symbol $\dot{\square} = \frac{\partial}{\partial t}\square$ denotes a time derivative.

The application of Hamilton's principle and integration by parts of Eqs. (13) leads to equations of motion associated with the 3-mode theory of torsional behaviour. These equations can written as a set of two following partial differential equations:

$$\begin{cases} A_1(x,t) + \frac{2}{3}a^2 A_3(x,t) + \frac{1}{2}a^4 A_5(x,t) = 0 \\ A_1(x,t) + \frac{3}{4}a^2 A_3(x,t) + \frac{3}{5}a^4 A_5(x,t) = 4\mu\vartheta_3(x,t) + 6\mu a^2\vartheta_5(x,t) \\ A_1(x,t) + \frac{4}{5}a^2 A_3(x,t) + \frac{2}{3}a^4 A_5(x,t) = 8\mu\vartheta_3(x,t) + \frac{64}{5}a^4\mu\vartheta_5(x,t) \end{cases} \tag{15}$$

where μ is the shear modulus and $A_1(x,t)$, $A_3(x,t)$ and $A_5(x,t)$ are auxiliary functions expressed as follows:

$$\begin{cases} A_1(x,t) = c_s^2\vartheta_1''(x,t) - \ddot{\vartheta}_1(x,t) \\ A_3(x,t) = c_s^2\vartheta_3''(x,t) - \ddot{\vartheta}_3(x,t) \\ A_5(x,t) = c_s^2\vartheta_5''(x,t) - \ddot{\vartheta}_5(x,t) \end{cases} \tag{16}$$

where c_s is the speed of shear elastic waves within a 3-D unbounded medium [25].

Equations (15) describe the beam motion according to the 3-mode theory of torsional behaviour and they couple spacial changes of the components ϑ_1, ϑ_3 and ϑ_5 of the tangential displacement u_θ with changes in time t. However, in order to obtain the dispersion curves, which express changes of the phase c_p and group c_g velocities as a function of the angular frequency ω or the frequency $f = \frac{\omega}{2\pi}$, for the three modes of elastic torsional waves associated with the 3-mode theory of torsional behaviour of the beam, the equations of motion (15) must be transformed from the time domain t into the frequency domain ω. For that purpose it is convenient to assume that the components ϑ_1, ϑ_3 and ϑ_5 can be expressed as solutions of the equations of motion:

$$\begin{cases} \vartheta_1(x,t) = \langle\vartheta_1\rangle \exp[-i(kx - \omega t)] \\ \vartheta_3(x,t) = \langle\vartheta_3\rangle \exp[-i(kx - \omega t)] \\ \vartheta_5(x,t) = \langle\vartheta_5\rangle \exp[-i(kx - \omega t)] \end{cases} \tag{17}$$

where $i = \sqrt{-1}$ is the imaginary unit and ω and k denote the angular frequency and the wave number, respectively.

A system of three linear homogeneous equations can be obtained for each harmonic amplitude component $\langle\vartheta_1\rangle$, $\langle\vartheta_3\rangle$ and $\langle\vartheta_5\rangle$ by simple substitution of Eqs. (17) into Eqs. (15) and some simplifications:

$$\begin{cases} (\omega^2 - c_s^2k^2)\langle\vartheta_1\rangle + \frac{2}{3}a^2(\omega^2 - c_s^2k^2)\langle\vartheta_3\rangle + \frac{1}{2}a^4(\omega^2 - c_s^2k^2)\langle\vartheta_5\rangle = 0 \\ (\omega^2 - c_s^2k^2)\langle\vartheta_1\rangle + \frac{3}{4}[a^2\omega^2 - c_s^2(a^2k^2 + \frac{16}{3})]\langle\vartheta_3\rangle + \frac{3}{5}a^2[a^2\omega^2 - c_s^2(a^2k^2 + 10)]\langle\vartheta_5\rangle = 0 \\ (\omega^2 - c_s^2k^2)\langle\vartheta_1\rangle + \frac{4}{5}[a^2\omega^2 - c_s^2(a^2k^2 + 10)]\langle\vartheta_3\rangle + \frac{2}{3}a^2[a^2\omega^2 - c_s^2(a^2k^2 + \frac{96}{5})]\langle\vartheta_5\rangle = 0 \end{cases} \tag{18}$$

This system has a non-trivial solution only when its determinant vanishes. This leads to a characteristic polynomial equation associated with the current problem:

$$(\omega^2 - c_s^2k^2)[a^4\omega^4 - 2a^2\omega^2(a^2k^2 + 120)c_s^2 + (a^4k^4 + 240a^2k^2 + 5760)c_s^4] = 0 \tag{19}$$

being a 6-th order polynomial equation with respect to the wave number k and being a function of the angular frequency ω. Depending on the angular frequency ω this characteristic polynomial can have three real and positive roots that represent three independent modes of elastic torsional waves that can propagate within the beam and which are allowed by the 3-mode theory of torsional behaviour. These roots can be calculated numerically for any chosen value of the angular frequency ω and thanks to the relationship $k = k(\omega)$ derived above, the phase velocity $c_p = \frac{\omega}{k}$ as well as the group velocity $c_g = \frac{d\omega}{dk}$ can be easily calculated and plotted. The same procedure was used by the authors to calculate the dispersion curves

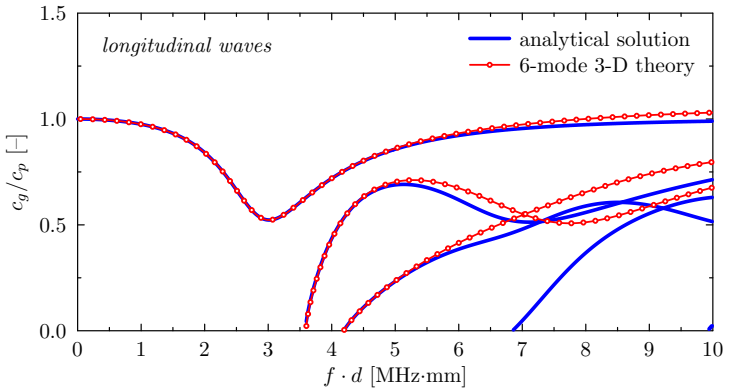

Figure 6: Dispersion curves of subsequent longitudinal modes for the group-to-phase velocity ratio c_g/c_p as a function of the frequency parameter $f \cdot d$, for a 6-mode theory of longitudinal behaviour of an isotropic beam.

associated with the 6-mode theory of longitudinal behaviour of the beam as well as the 8-mode theory of flexural behaviour, presented and discussed in the previous section of the paper. The results obtained by the authors are shown in Figs. 6–8 as a function of a frequency parameter $f \cdot d$, where $d = 2a$ is the beam diameter.

It can be seen from Figs. 6–8 that the three theories of the beam dynamic behaviour (i.e. longitudinal, flexural and torsional) considered by the authors agree very well with corresponding analytical solutions in the range of the frequency parameter f·d up to 5 MHz·mm. The dispersion curves presented in Fig. 6 indicate that in the case of the 6-mode theory of longitudinal behaviour only three modes of elastic longitudinal waves can propagate within this range of the frequency parameter $f \cdot d$. The maximal relative error between the analytical solution and the 6-mode theory of longitudinal behaviour reaches 2% at 5 MHz·mm in the case of the second mode. According to the dispersion curves presented in Fig. 7 the same number of modes is available for propagation of elastic flexural waves in the case of the 8-mode theory of flexural behaviour. The maximal relative error between the analytical solution and the 8-mode theory of flexural behaviour reaches 1% at 5 MHz·mm in the case of the third mode. Finally, in the case of the 3-mode theory of torsional

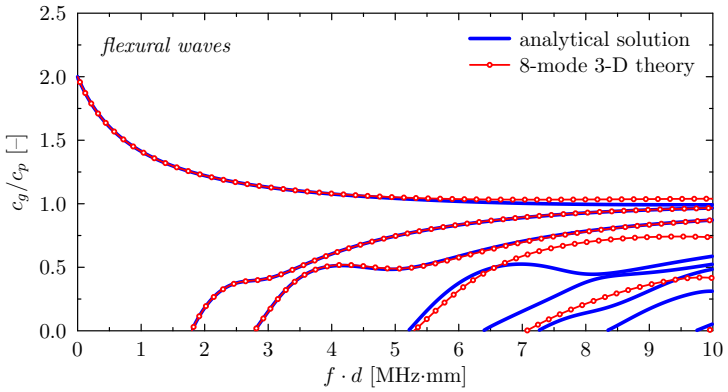

Figure 7: Dispersion curves of subsequent flexural modes for the group-to-phase velocity ratio c_g/c_p as a function of the frequency parameter $f \cdot d$, for a 8-mode theory of flexural behaviour of an isotropic beam.

behaviour of the beam only one mode of elastic torsional waves can propagate within the range of the frequency parameter $f \cdot d$ up to 5 MHz·mm, as shown in Fig. 8. The relative error between the analytical solution and the 3-mode theory of torsional behaviour of the beam is practically negligible in the case of the first mode.

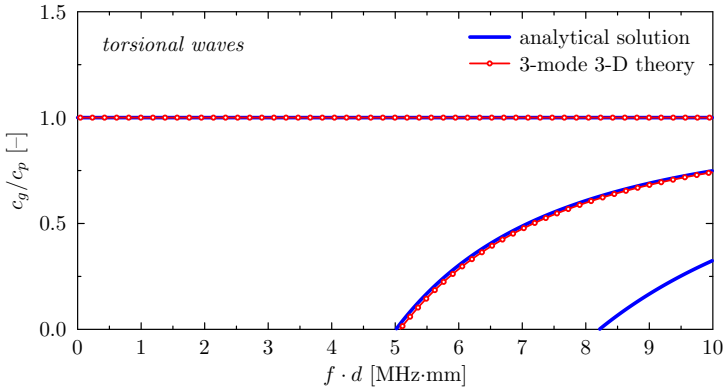

Figure 8: Dispersion curves of subsequent torsional modes for the group-to-phase velocity ratio c_g/c_p as a function of the frequency parameter $f \cdot d$, for a 3-mode theory of torsional behaviour of an isotropic beam.

4. Initial numerical computations

The results of numerical computations presented in the following section were obtained by the authors by the use of the SFEs developed and described above. They aim to demonstrate the influence of the beam geometry on the presence, positions and widths of the frequency band gaps in the natural frequency spectra of the beam under investigation. For that purpose it was assumed that regardless of the type of vibrations the beam was divided into 200 SFEs (i.e. 200 SFEs = 5 SFEs/cell × 40 cells), which resulted in 1001 nodes.

Depending on the type of analysis the number of degrees of freedom (DOF) of the numerical model employed by the authors varied. This number was equal to 6006, 8008 and 3003 DOF in the case of the analysis of longitudinal, flexural and torsional natural vibrations of the beam, respectively.

In order to demonstrate the influence of the cell geometry on the natural frequencies of the beam two different calculation scenarios were considered. In the first scenario the variation of the radius $r_i(\xi)$ within a single cell was described by the discrete values of $r_i = \{5, 6.25, 7.5, 8.75, 10, 5\}$ mm, as presented in Fig. 9(a). In the second scenario the magnitude of the radius variation was increased by 50%, which resulted

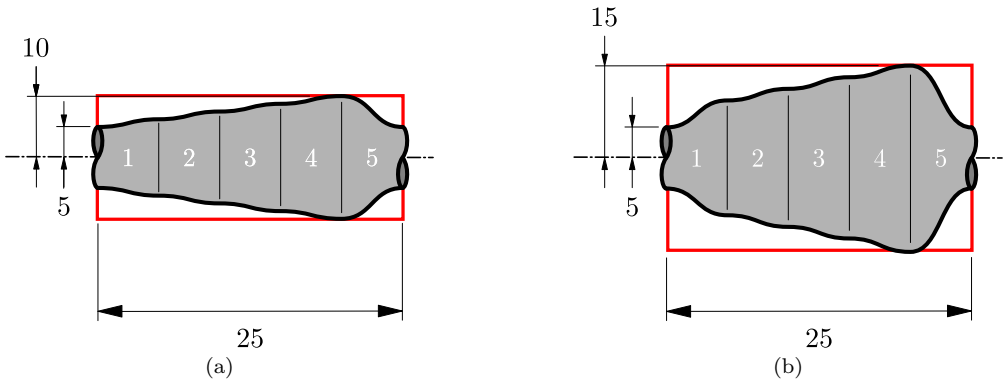

Figure 9: Geometry of a single cell modelled by 5 SFEs, described by the discrete values $r_i = \{5, 6.25, 7.5, 8.75, 10, 5\}$ mm (a), and $r_i = \{5, 7.5, 10, 12.5, 15, 5\}$ mm (b), considered for numerical calculations of natural frequency spectra of a periodic beam by the use of TD-SFEM.

in the discrete values of $r_i = \{5, 7.5, 10, 12.5, 15, 5\}$ mm, as presented in Fig. 9(b). It should be noted here that the values of r_1 and r_6 remained unaffected and were equal to 5 mm.

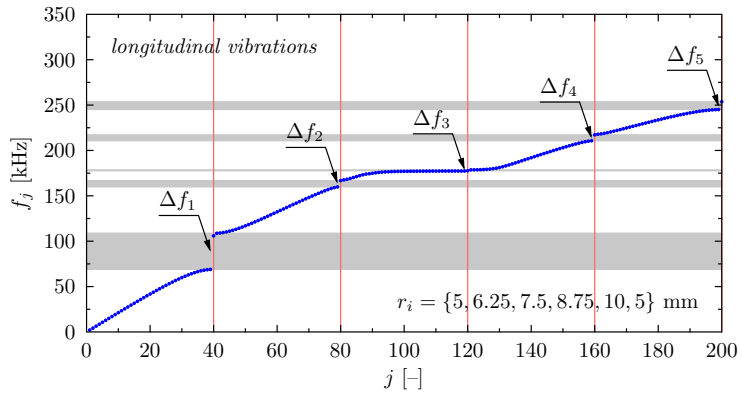

Figure 10: Spectrum of natural frequencies associated with longitudinal vibrations of a periodic beam as a function of natural frequency number j. Results obtained numerically by the use of TD-SFEM and based on the 6-mode theory of longitudinal behaviour of the beam.

A typical result depicting changes in the spectrum of natural frequencies of the beam in the case of longitudinal vibrations is presented in Fig. 10. It can be clearly seen from Fig. 11 that periodic variations of the beam cross-section lead to visible changes in its natural frequency spectra, manifesting in the presence of so-called frequency band gaps, despite non-periodic boundary conditions of the beam. It should be remembered here that the free type of boundary conditions were used instead. This concerns all types of natural vibrations: longitudinal, flexural and torsional. Moreover, it should be noted that in the current case the spectrum of torsional natural vibrations is mostly affected by the presence of frequency band gaps and they can be characterised by the greatest widths, which can be easily seen in Fig. 11. In this figure, for clarity of the presentation, only the positions and widths of particular frequency band gaps are shown, for all three types of beam natural vibrations considered.

It should be emphasised that the positions of particular frequency band gaps in the natural frequency spectra of the beam under investigation are closely correlated with the number of cells N within the beam, which in the current case is equal to 40. The number of cells N defines the beam periodicity. The frequency band gaps, noted in the figures as $\Delta f_m (m = 1, 2, 3, \ldots)$, appear at multiples of the cell number N. Among all frequency band gaps $\Delta f_m (m = 1, 2, 3, \ldots)$ the primary ones Δf_1 are characterised by the greatest widths, except the longitudinal natural vibrations, where the greatest widths have the frequency band gaps Δf_2.

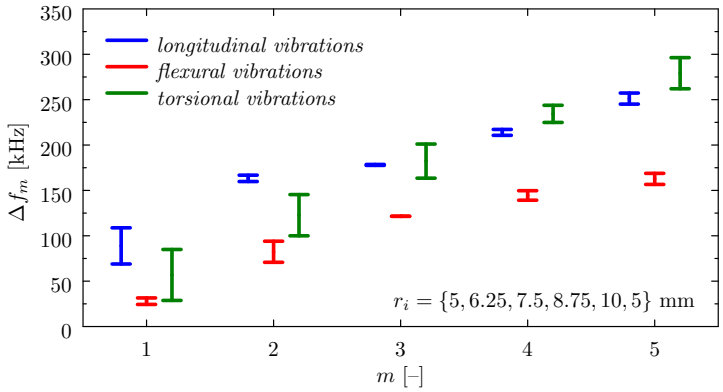

Figure 11: Changes in the positions and widths of frequency band gaps Δf_m as a function of the frequency band gap number m, in the case of: longitudinal (blue), flexural (red) and torsional (green) natural vibrations of a periodic beam. Results obtained numerically by the use of TD-SFEM and based on the: 6-mode theory of longitudinal behaviour, 8-mode of flexural behaviour as well as 3-mode of torsional behaviour of the beam, for the discrete values of $r_i = \{5, 6.25, 7.5, 8.75, 10, 5\}$ mm.

An increase in the magnitude of the radius variation resulted not only in widening of particular frequency band gaps $\Delta f_m = f_{Nm+1} - f_{Nm}$, but also in changes of their positions $\bar{f}_m (m = 1, 2, 3, \ldots)$ in the natural frequency spectra defined as $\bar{f}_m = \frac{1}{2} f_{Nm+1} + \frac{1}{2} f_{Nm}$. The only unaffected feature is their positions with respect to the frequency number j, as directly resulting from the periodicity of the beam, which remains the same and equal to N, as is clearly seen in Fig. 12.

It can be seen from Fig. 11 and Fig. 12 that for longitudinal natural vibrations the width Δf_1 and position $\bar{f}_1$ of the first frequency band gap changed from 39.9 kHz at 88.9 kHz to 50.9 kHz at 75.6 kHz. In the case of flexural vibrations they changed from 8.2 kHz at 27.4 kHz to 10.5 kHz at 23.3 kHz, while in the case of torsional vibrations the change was from 56.2 kHz at 56.8 kHz to 73.3 kHz at 52.6 kHz. The width Δf_2 and position $\bar{f}_2$ of the second frequency band gap in the spectrum of natural frequencies, associated with flexural vibrations, changed more prominently from 23.4 kHz at 82.5 kHz to 33.4 kHz at 63.52 kHz.

The results of numerical computations presented in Fig. 11 and Fig. 12 allow the authors to conclude that through careful manipulation of the cell geometry it should be possible to adjust not only the width, but also the position of particular frequency band gaps in the spectra of natural frequencies of the beam. In this way dynamic characteristics of the beam could be optimised in order to achieve desired isolation or filtering properties.

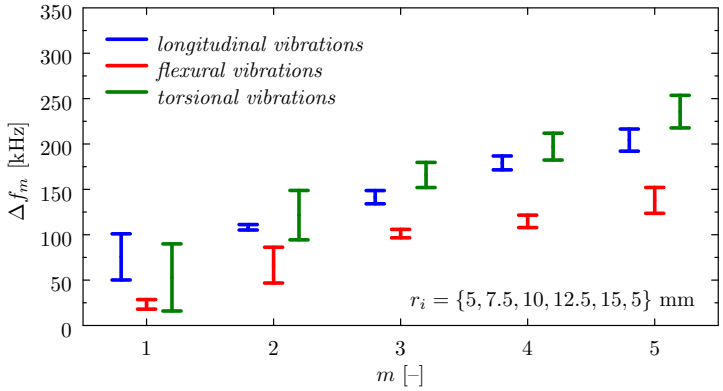

Figure 12: Changes in the positions and widths of frequency band gaps Δf_m as a function of the frequency band gap number m, in the case of: longitudinal (blue), flexural (red) and torsional (green) natural vibrations of a periodic beam. Results obtained numerically by the use of TD-SFEM and based on the 6-mode theory of longitudinal behaviour, 8-mode of flexural behaviour as well as 3-mode of torsional behaviour of the beam, for the discrete values of $r_i = \{5, 7.5, 10, 12.5, 15, 5\}$ mm.

For this reason it was assumed by the authors that the geometry of the beam can be optimised in the context of the position and the width of one common frequency band gap in the natural frequency spectra of the beam. Three different positions of the common frequency band gap $\bar{f}_c$ equal to 20 kHz, 40 kHz as well as 60 kHz were considered here, all of the same width $\Delta f_c = 10$ kHz.

The optimisation procedure employed by the authors in this paper is presented in the following section *Optimisation procedure*. The results of the optimisation process employed by the authors are discussed in detail in the subsequent section *Numerical and experimental verification*. They concern and confirm not only the correspondence of numerical simulation results and experimental measurements obtained by the authors, but also their correctness.

5. Optimisation procedure

As before, the frequency band gaps of the beam are denoted as $\Delta f_m (m = 1, 2, 3, \ldots)$. A target frequency band to be covered by these band gaps is Δf_c and is allocated symmetrically with respect to the target central frequency f_0. The lower and upper frequencies defining the band gaps $\Delta f_m (m = 1, 2, 3, \ldots)$ are denoted as f_{m_1} and f_{m_2}, as well as by f_{c_1} and f_{c_2} as the frequencies defining the target band Δf_c. In that context the optimisation problem can be defined as a problem to adjust the vector $\mathbf{r} = [r_1 \ldots r_6]^T$ in order to obtain a maximal coverage of the target band by the frequency band gaps of the beam and, at the same time, minimal (possibly zero) coverage of the remaining part of the spectrum. This optimisation problem can be stated as:

$$\mathbf{r}^* = \arg\min_{\mathbf{r}} U(\mathbf{r}) \tag{20}$$

The scalar objective function $U(\mathbf{r})$ is defined by considering the following three cases:

1. If $[f_{m_1} f_{m_2}] \cap [f_{c_1} f_{c_2}] = \varnothing$ for $m = 1, 2, 3, \ldots$, i.e. when there is no overlap between the band gaps. In this case the value of the objective function is $U(\mathbf{r}) = \min\{m : d_m\}$, where $d_m = f_{c_1} - f_{m_2}$ if $f_{m_2} < f_{c_1}$ or alternatively $d_m = f_{m_1} - f_{c_2}$ if $f_{m_1} > f_{c_2}$. In other words, the objective is the minimum distance between the target frequency band and the closest band gap. The objective function value can be positive or is zero in the cane when one of the band gaps is adjacent to the target frequency band.
2. If $[f_{m_1} f_{m_2}] \cap [f_{c_1} f_{c_2}] = \varnothing$ for at least one m, the the objective is defined as $M(f_{c_1} - f_{c_2})$, where M is a fraction of the target band, which is covered by the band gaps, assuming that $M < 1$. In this case the maximum value of the objective function is zero, whereas the minimum is $f_{c_1} - f_{c_2}$.
3. If $\cup_m [f_{m_1} f_{m_2}] \cap [f_{c_1} f_{c_2}] = [f_{c_1} f_{c_2}]$, i.e. when the target frequency band is entirely covered by the band gaps then the objective is defined as $(f_{c_1} - f_{c_2})(2 - P)$, with P being defined as $\sum_m [(f_{m_2} - f_{m_1}) - (f_{c_2} - f_{c_1})]/[\Delta f - (f_{c_2} - f_{c_1})]$, and where Δf is the entire frequency range under consideration. Thus, P is a fraction of the frequency spectrum, except the target band, which is covered by the band gaps. Here, the objective function value can be between $f_{c_1} - f_{c_2}$ and $2(f_{c_1} - f_{c_2})$.

The above definition of the objective function is introduced to distinguish three qualitatively different situations, and order them in terms of a decreasing value of the objective function. On the one hand, one is interested in obtaining possibly large coverage of the target band. On the other hand, the band gaps should be reduced to the target band as much as possible. The best possible situation is a complete coverage of the target band and no band gaps anywhere else within the frequency spectrum at the same time.

The problem defined by Eq. (20) with the objective function $U(\mathbf{r})$, in conjunction with the beam vibration model, is a difficult multi-modal task. The optimisation engine of choice is a particle swarm optimiser (PSO) [28], being the global optimisation routine, followed by a pattern search algorithm, being the local optimiser. The details of the pattern search algorithm can be found in [29]. A brief exposition of the PSO routine is provided here for the convenience of all potential readers.

PSO is based on mimicking the swarm behaviour exhibited in nature, such as the schooling of fish or the flocking of birds [28]. It simulates a set of individuals that interact with each other using social influence and social learning. A typical model of the swarm is particles represented by their positions and velocities, i.e. certain vectors. The particles exchange information about good positions, in terms of the corresponding objective function value, and adjust their own velocity and position accordingly. The particle movement has

two components: stochastic and deterministic. Each particle is attracted toward the position of the current global best position $\mathbf{g}$ and its own best location $\mathbf{r}_i^*$ found during the optimization run. At the same time, it has a tendency to move randomly.

Let $\mathbf{r}_i$ and $\mathbf{v}_i$ denote the position and the velocity vectors of the i-th particle. Both vectors are updated according to the following rules:

$$\begin{cases} \mathbf{v}_i \leftarrow \chi[\mathbf{v}_i + c_i\mathbf{R}_1 \bullet (\mathbf{r}_i^* - \mathbf{r}_i) + c_2\mathbf{R}_2 \bullet (\mathbf{g} - \mathbf{r}_i)] \\ \mathbf{r}_i \leftarrow \mathbf{r}_i + \mathbf{v}_i \end{cases} \tag{21}$$

where $\mathbf{R}_1$ and $\mathbf{R}_2$ are vectors with components being uniformly distributed random numbers between 0 and 1, whereas $\bullet$ denotes component-wise multiplication. The parameter χ is set to 0.7298 [28], while c_1 and c_2 are acceleration constants determining how much a particle is directed towards good positions. They represent a *cognitive* component and a *social* component, respectively. In the current case they are equal to $c_1 = 2.0$ and $c_2 = 2.1$. The sum of $c_1 + c_2$ should not be smaller than 4.0 [28]. As the values of the parameters c_1 and c_2 increase, χ gets smaller, as also does the damping effect. In the present implementation the size of the swarm was set to 80 and the maximal number of iterations to 100.

It should be emphasised that having the control parameters c_1 and c_2 at these values (i.e. $c_1 + c_2$ above 4.0 as a sum) is a general recommendation following the analysis of PSO as a dynamical system [28]. In particular, this ensures that the damping effects due to directing the particles towards good positions are at the sufficient level. If this is not the case, the search may turn into the random search (in particular, if $c_1 + c_2$ is too small) or one can experience premature convergence (if $c_1 + c_2$ is too large).

6. Numerical and experimental verification

6.1. Computations by TD-SFEM

As a result of the optimisation procedure described above three sets of the discrete values of r_i were obtained by the authors for a predefined width of the common frequency band Δf_c equal to 10 kHz. In each of these cases the common frequency band gap Δf_c was positioned within the natural frequency spectra of the beam under investigation at a different central frequency $\bar{f}_c$ equal to 20 kHz, 40 kHz and 60 kHz, for all three types of beam natural vibrations: longitudinal, flexural and torsional, respectively. This is summarised in Tab. 1.

Table 1: Discrete values of $r_i (i = 1, 2, \ldots, 6)$ resulted from the optimisation procedure of the beam geometry for predefined positions of the common frequency band gap $\bar{f}_c$ of a constant width Δf_c equal to 10 kHz within natural frequency spectra of the beam, in the case of longitudinal, flexural and torsional behaviour. Results obtained numerically by the use of TD-SFEM and based on the 6-mode theory of longitudinal behaviour, 8-mode of flexural behaviour, as well as 3-mode of torsional behaviour of the beam.

	$\bar{f}_c$ [kHz]	Δf_c [kHz]	r_1 [mm]	r_2 [mm]	r_3 [mm]	r_4 [mm]	r_5 [mm]	r_6 [mm]
1	20	10	7.6	37.2	27.8	37.2	7.7	7.6
2	40	10	11.2	26.4	18.7	28.7	14.7	11.2
3	60	10	9.9	16.4	19.8	14.6	31.8	9.9

The results of numerical simulation by the use of TD-SFEM, based on the presented theories of the beam longitudinal, flexural and torsional behaviour, and corresponding to the three sets of the discrete values of r_i are shown in Figs. 13–15. In Fig. 13 they are presented for the value of $\bar{f}_c = 20$ kHz, in Fig. 14 for the value of $\bar{f}_c = 40$ kHz, and in Fig. 15 for the value of $\bar{f}_c = 60$ kHz. In each of these cases the position of the common frequency band gaps Δf_c equal to 10 kHz is indicated by a grey colour band.

It is clearly seen from Figs. 13–15 that in each of the cases considered here the presence of one common frequency band gap Δf_c is a direct consequence of overlapping of some of the existing frequency band gaps $\Delta f_m (m = 1, 2, 3, \ldots)$ within the natural frequency spectra of of the beam.

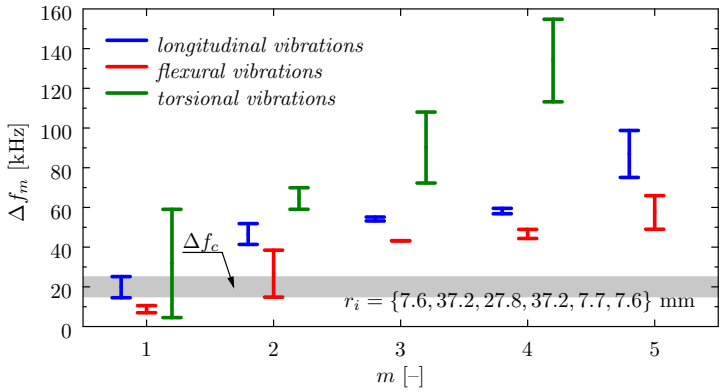

Figure 13: Changes in the positions and widths of frequency band gaps Δf_m as a function of the frequency band gap number m, in the case of: longitudinal (blue), flexural (red) and torsional (green) natural vibrations of a periodic beam of optimised geometry. A common frequency band gap Δf_c of 10 kHz centrally positioned in the frequency spectra of the beam at 20 kHz. Results obtained numerically by the use of TD-SFEM and based on the 6-mode theory of longitudinal behaviour, 8-mode of flexural behaviour, as well as 3-mode of torsional behaviour of the beam, for the discrete values of $r_i = \{7.6, 37.2, 27.8, 37.2, 7.7, 7.6\}$ mm.

For the first scenario and the common frequency band gap Δf_c centrally positioned in the frequency spectra of the beam at 20 kHz, it is evident from Fig. 13 that its existence results from overlapping of the first frequency band gap in the case of longitudinal vibrations (within the range of natural frequencies from 14.5 kHz to 25.2 kHz), the first frequency band gap in the case of torsional vibrations (within the range of natural frequencies from 4.5 kHz to 59.0 kHz), as well as the second frequency band gap in the case of the flexural vibrations (within the range of natural frequencies from 14.8 kHz to 38.5 kHz).

In a similar manner, for the second scenario and the frequency band gap Δf_c centrally positioned in the frequency spectra of the beam at 40 kHz, it is clear from Fig. 14 that the presence of one common frequency band gap Δf_c results from overlapping of the same set of frequency band gaps. These are the first frequency band gap in the case of longitudinal vibrations (within the range of natural frequencies from 34.8 kHz to 45.1 kHz), the first frequency band gap in the case of torsional vibrations (within the range of natural frequencies from 17.1 kHz to 51.5 kHz), as well as the second frequency band gap in the case of the flexural vibrations (within the range of natural frequencies from 31.0 kHz to 50.8 kHz).

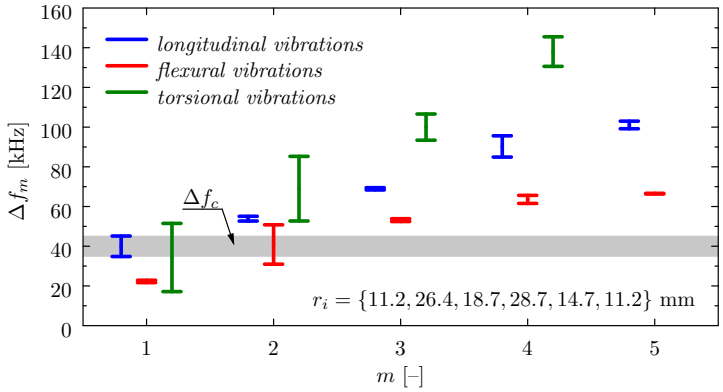

Figure 14: Changes in the positions and widths of frequency band gaps Δf_m as a function of the frequency band gap number m, in the case of: longitudinal (blue), flexural (red) and torsional (green) natural vibrations of a periodic beam of optimised geometry for the common frequency band gap Δf_c of 10 kHz centrally positioned in the frequency spectra of the beam at 40 kHz. Results obtained numerically by the use of TD-SFEM and based on the 6-mode theory of longitudinal behaviour, 8-mode of flexural behaviour as well as 3-mode of torsional behaviour of the beam, for the discrete values of $r_i = \{11.2, 26.4, 18.7, 28.7, 14.7, 11.2\}$ mm.

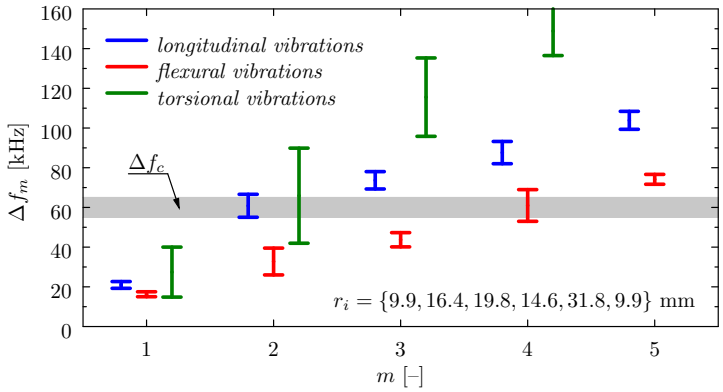

Figure 15: Changes in the positions and widths of frequency band gaps Δf_m as a function of the frequency band gap number m, in the case of: longitudinal (blue), flexural (red) and torsional (green) natural vibrations of a periodic beam of optimised geometry for the common frequency band gap Δf_c of 10 kHz centrally positioned in the frequency spectra of the beam at 60 kHz. Results obtained numerically by the use of TD-SFEM and based on the 6-mode theory of longitudinal behaviour, 8-mode of flexural behaviour as well as 3-mode of torsional behaviour of the beam, for the discrete values of $r_i = \{9.9, 16.4, 19.8, 14.6, 31.8, 9.9\}$ mm.

Due to a higher value of the central position $\bar{f}_c$ of the common frequency band gap Δf_c positioned at 60 kHz, the third scenario involves frequency band gaps $\Delta f_m (m = 1, 2, 3, \ldots)$ also positioned higher in the natural frequency spectra of the beam. It can be seen from Fig. 15 that the existence of the common frequency band gap Δf_c results this time from overlapping of the second frequency band gap in the case of longitudinal vibrations (within the range of natural frequency 55.0 kHz to 66.6 kHz), the second frequency band gap in the case of torsional vibrations (within the range of natural frequencies from 42.0 kHz to 89.9 kHz), as well as the fourth frequency band gap in the case of the flexural vibrations (within the range of natural frequencies from 53.0 kHz to 69.0 kHz).

6.2. Computations by FEM

The results of numerical computations obtained by the authors using TD-SFEM and the spectral finite elements developed in the case of the longitudinal, flexural and torsional behaviour of the periodic beam under investigation were cross-verified by the use of the classical FEM. Due to the size of the numerical model required for this purpose, resulting from full 3-D modelling of the beam, as well as meshing requirements [18] resulting from high frequency responses sought, only the first scenario was considered here, when the common frequency band gap Δf_c of 10 kHz was centrally positioned in the frequency spectra of the beam at 20 kHz.

As a numerical tool the Autodesk Simulation Mechanical FEM software was selected by the authors. The beam was modelled by more than 1.2 million 4-node tetrahedral FEs of linear shape functions. The numerical model included more than 250 thousand nodes in total, which was equivalent to more than 770 thousand DOFs. Numerical computations considered calculations of the first 200 modes of natural vibrations of the beam in the frequency range up to 26 kHz. Also in this case the free type of boundary conditions were used by the authors.

A detailed view of a single unit cell divided into FEs for numerical calculations by FEM is presented in Fig. 16. It should be emphasised here that a numerical model of a single unit cell had to be very rich in order to appropriately represent locally high frequency responses of the beam at high frequencies, especially around these natural frequencies, which were close to the central frequency $\bar{f}_c$ of the common frequency band gap Δf_c. This model included more than 30 thousand 4-node tetrahedral FEs, which resulted in 47 thousand nodes, which is equivalent to 141 thousand DOFs.

It was expected that, in a similar manner as in the case of numerical computations by TD-SFEM, a visible frequency band gap Δf_c of approximately 10 kHz, around the central frequency $\bar{f}_c$ of 20 kHz, should be observable also in this instance. It was found that such a frequency band gap exists between modes of

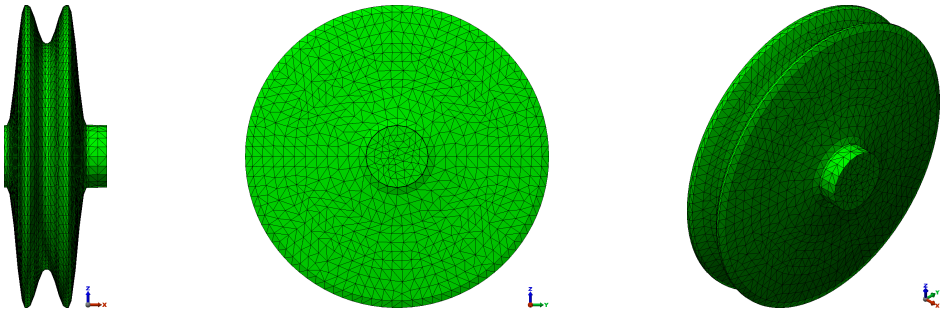

(a) (b) (c)

Figure 16: A detailed view: side (a), front (b), perspective (c), of a single unit cell divided into FEs for numerical calculations using the classical FEM employing 4-node tetrahedral FEs provided by Autodesk Simulation Mechanical FEM software.

natural vibrations 180 and 181 and concerns frequencies of natural vibrations equal to 15.86 kHz and 25.51 kHz, respectively, as is clearly seen in Fig. 17. Thus, the resulting frequency band gap was equal to 9.65 kHz and it was positioned around the central frequency equal to 20.69 kHz. This is equivalent to the relative error of 3.5% for both these values.

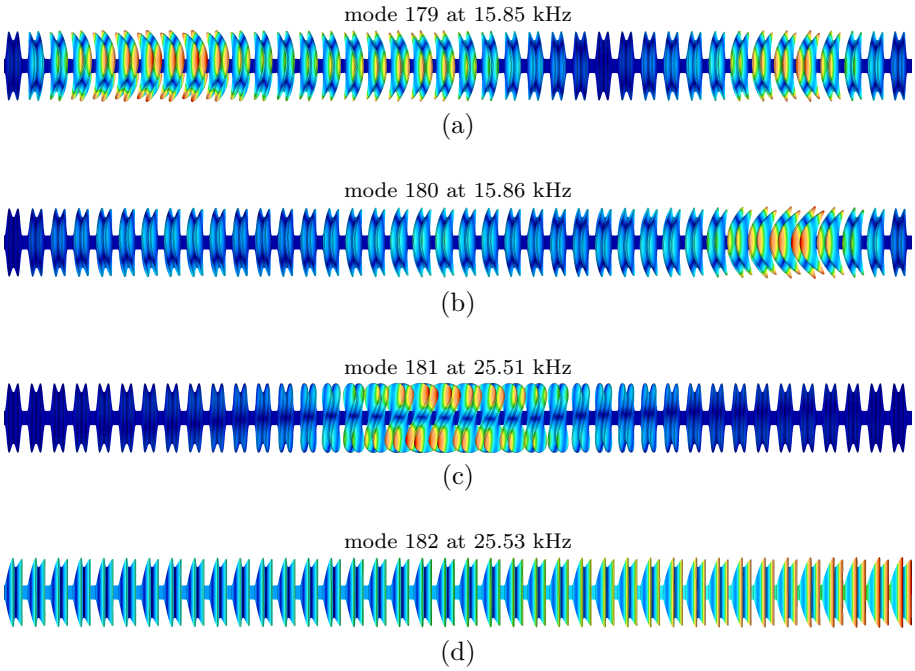

Figure 17: Selected modes of natural vibrations of a periodic beam: mode 179 at 15.85 kHz (a), mode 180 at 15.86 kHz (a), mode 181 at 25.51 kHz (c), mode 182 at 25.53 kHz (d), calculated numerically by the classical FEM and application of 4-node tetrahedral FEs using Autodesk Simulation Mechanical FEM software.

In the opinion of the authors the primary source of this error comes from the inappropriate approximation of the beam geometry, which was initially assumed as smooth [30]. The condition of a smooth geometry could not be met in the classical FEM using the 4-node tetrahedral elements of linear or higher order shape functions. It should be noted that this particular condition is very difficult to meet using any FEM software available and in practice requires developing customised FEs, as was done by the authors. An additional source of the error may come from the fact that the 4-node tetrahedral FEs are better suited for solving static or low frequency dynamic problems [11] rather than high frequency dynamic responses.

6.3. Experimental measurements

The programme of experimental measurements was planned by the authors to verify not only the results of numerical investigations obtained by the use of TD-SFEM, presented in the previous section of this paper, and the results of the optimisation procedure that led to three different beam geometries, but primarily to verify the correctness of the concept discussed throughout the paper. However, due to very complex geometries resulting from the optimisation procedure as well as machining difficulties, the authors decided to test experimentally only one scenario, i.e. the case, for which the common frequency band gap Δf_c of 10 kHz was centrally positioned in the frequency spectra of the beam at 20 kHz.

Dynamic responses of the beam under investigation were measured experimentally in the form of the spectrum of forced vibrations as well as wave propagation patterns. For that purpose a one-dimensional (1-D) laser Doppler scanning vibrometer (LDSV) was used, model Polytec PSV-400. This system was additionally equipped with a linear amplifier, American Piezo, Inc. model EPA-140 (±200 Vpp). In order to induce beam vibrations during the experiments an American Piezo, Inc. PZT-850 transducer in the form of a disc (10 mm ×10 mm) was used. This transducer was attached eccentrically to the face of the first unit cell. The periodic beam, as well as the experimental equipment used by the authors, are presented in Fig. 18.

During the experiments only the radial component $\dot{u}_r$ of beam vibrations was measured by 1-D LDSV. Starting from the 1st unit cell the points located at the centre of the carving of every fifth unit cell were chosen as measurement points. In this manner 9 measurement points were selected. Vibrational signals at each measurement point were averaged based on 15 measurements.

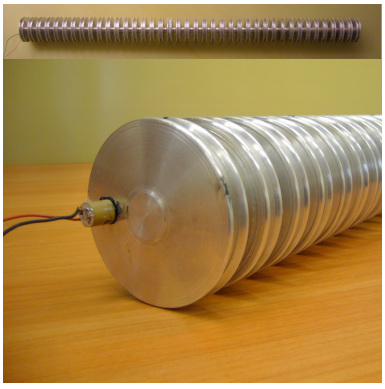

(a)

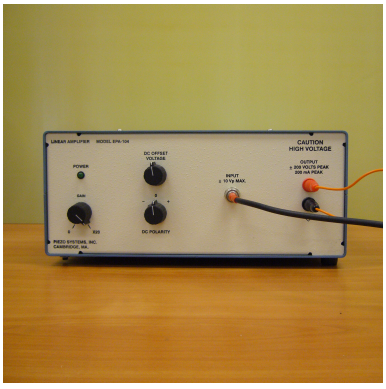

(b)

(c)

(d)

Figure 18: A detailed view of: a periodic beam sample with an American Piezo, Inc. PZT transducer attached (a), American Piezo, Inc. linear amplifier model EPA-140 (b), Polytec 1-D LDSV head (c), LDSV measurement unit model PSV-400 (d), used by the authors for experimental measurements.

The first measurement scenario concerned forced vibration responses of the beam. In this case the chirp type of excitation was used in the range of frequencies starting from 1 kHz up to 75 kHz. The results obtained from experimental measurements are presented in Fig. 19. These results should be understood as an averaged result from all 9 vibration spectra obtained from each measurement point.

It can be clearly seen from Fig. 19 that the position and the width of the common frequency band gap in the frequency spectrum of the beam very well corresponds to the values obtained by to the optimisation procedure. The common frequency band gap of the beam is located in Fig. 19 within the range of frequencies from 15.4 kHz to 25.7 kHz. This means that the total width of the frequency band gap Δf_c measured experimentally was 10.3 kHz, in comparison to its value obtained as the result of the optimisation procedure, equal to 10.4 kHz. In a similar manner the position of the centre of the experimentally measured frequency band gap $\bar{f}_c$ was 20.6 kHz, in comparison to its value obtained as the result of the optimisation procedure equal to 20.0 kHz. As a result the error related to the width of the common frequency band gap is smaller than 1%, while the error related to its position in the frequency spectrum of the beam is smaller than 3%. In the opinion of the authors this indicates that agreement between the experimental and numerical results is excellent.

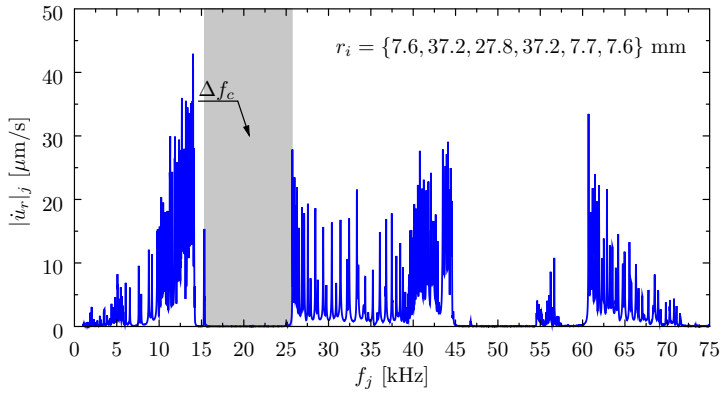

Figure 19: Spectrum of natural frequencies of a periodic beam measured experimentally by the use of 1-D LDSV, for the radial component $\dot{u}_r$ of beam vibrations, for the discrete values of $r_i = \{7.6, 37.2, 27.8, 37.2, 7.7, 7.6\}$ mm. A common frequency band gap Δf_c of 10.3 kHz centrally positioned in the frequency spectra of the beam at 20.5 kHz.

Moreover, the authors suspect that the small discrepancy observed could have its source primarily in machining of the experimental sample, and secondly in the values of material mechanical properties used for all numerical calculations, which could slightly differ from real values. Additionally, it could be relevant that precise machining of the beam sample required its division into two separate and equal parts that later had to be connected together by a specially designed aluminium bolt made from the same material.

The second measurement scenario concerned wave propagation patterns. It was assumed here that the total time T of each measurement was equal to 12.5 ms. The number of samples n collected at each measurement point was 1600. The sampling frequency f_s was 128 kHz and particular measurements were delayed in respect to each other by 1 s. It was expected by the authors that as a benefit of the optimised geometry of the beam its vibroacoustic isolation properties should have a significant influence on the propagation of elastic waves along the beam. Therefore three different frequencies of the excitation signal were selected by the authors, having different positions with respect to the common frequency band gap Δf_c. The excitation signals had a form of a sine pulse modulated by the Hann window. In each case the number of sine cycles m was equal to 5. The carrier frequencies f_c of the excitation were selected as 10 kHz, 20 kHz as well as 30 kHz, and the resulting modulation frequencies $f_m = f_c/m$ were equal to 2 kHz, 4 kHz and 6 kHz. The time and frequency domain shapes of the excitation signal in the case of the excitation frequency f_c of 10 kHz and the modulation frequency of f_m of 2 kHz, are presented in Fig. 20.

It should be understood that depending on the carrier and modulation frequencies f_c and f_m a part of the signal energy can fall into the common frequency band gap Δf_c. In the current case of the carrier frequency f_c of 10 kHz signal energy is carried within the range of frequencies starting from $f_c - 2f_m$ equal

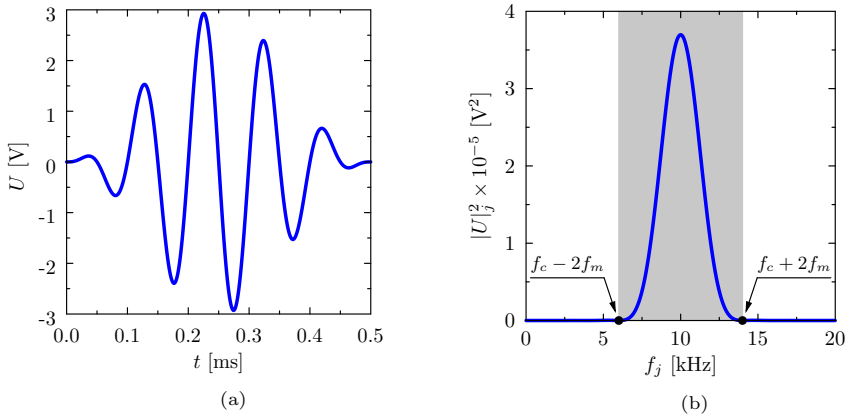

Figure 20: Typical variation of an excitation voltage signal applied to a PZT transducer during experimental measurements: in the time domain (a), in the frequency domain (b).

to 6 kHz up to $f_c + 2f_m$ equal to 14 kHz, therefore practically no signal energy falls into the common frequency band gap. In the case of the carrier frequency f_c of 20 kHz signal energy is carried within the range of frequencies starting from $f_c - 2f_m$ equal to 12 kHz up to $f_c + 2f_m$ equal to 28 kHz, and 97.4% of the signal energy falls into the common frequency band gap. Finally, in the case of the carrier frequency f_c of 30 kHz signal energy is carried within the range of frequencies starting from $f_c - 2f_m$ equal to 18 kHz up to $f_c + 2f_m$ equal to 42 kHz, and only 7.6% of signal energy falls into the common frequency band gap. As a consequence of this it can be expected that vibroacoustic isolation properties of the beam observed and measured, based on wave propagation patterns of the radial component $\dot{u}_r$ of beam vibrations, should differ and appear as strongly dependent on the value of the carrier frequency f_c. This is well illustrated by Fig. 21, Fig. 22 and Fig. 23.

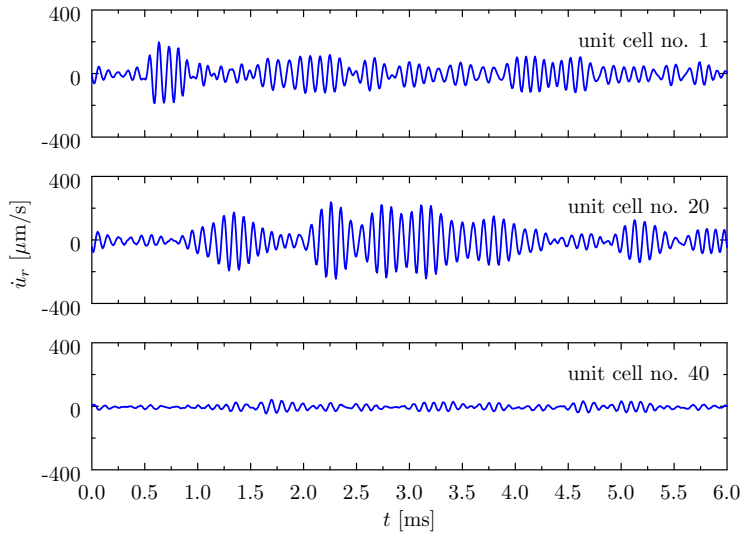

Figure 21: Wave propagation patters of a periodic beam measured experimentally by the use of 1-D LDSV, for the radial component $\dot{u}_r$ of beam vibrations, for the discrete values of $r_i = \{7.6, 37.2, 27.8, 37.2, 7.7, 7.6\}$ mm. Results obtained for the carrier frequency f_c of the excitation signal equal to 10 kHz outside the common frequency band gap Δf_c.

It can be clearly seen from Fig. 21, Fig. 22 and Fig. 23 that the value of the excitation frequency f_c, with respect to the position and width of the common frequency band gap of the beam Δf_c, has a great impact on the wave propagation patterns that can be observed. In the case of the excitation frequency f_c of

10 kHz it can be noted that the maximum amplitude of the radial component $\dot{u}_r$ of beam vibrations in the 1st unit cell reaches 197.4 μm, while its value in the 40th unit cell drops down to 45.9 μm. This is equivalent to a relative change of 76.8%. In the case of the excitation frequency f_c of 20 kHz the changes observed are significantly different. The maximum amplitude of the radial component $\dot{u}_r$ of beam vibrations in the 1st unit cell reaches 829.8 μm, while its value in the 40th unit cell drops down to 11.7 μm, which is equivalent to a relative change of 98.6%. Finally, in the case of the excitation frequency f_c of 30 kHz the maximum amplitude of the radial component $\dot{u}_r$ of beam vibrations in the 1st unit cell reaches 226.2 μm, while its value in the 40th unit cell drops down to 34.3 μm. This is equivalent to a relative change of 84.8%.

Obviously, when the frequency range of the excitation signals falls outside the common frequency band gap, as in the case of results presented in Fig. 21 and Fig. 23, changes in the wave propagation patterns result only from internal cross-reflection of the signal as well as natural damping properties of the beam material. The latter was not taken into account by the authors. In contrast to this, when the frequency range of the excitation signals falls into the common frequency band gap, the vibroacoustic isolation properties of the beam manifest very strongly, as presented in the case of Fig. 22. It should be emphasised that the relatively strong damping of signals propagating along the beam in the case of the carrier frequency f_c of 30 kHz, higher than in the case of the carrier frequency f_c of 10 kHz, in the opinion of the authors can be attributed to the fact that still 7.6% of the signal energy falls into the common frequency band gap.

In order to better illustrate this property of the beam, the results obtained by the authors are presented in Fig. 24 as the values of a damping coefficient ζ_j at selected measurement points j, measured with respect to the power of the signal measured at the 1st unit cell, and for the carrier frequencies f_c of the excitation signals equal 10 kHz, 20 kHz as well as 30 kHz. The value of the damping coefficient ζ_j was calculated by the authors according to the following simple formula:

$$\zeta_j = 10 \log_{10} \frac{p_j}{p_1}, \quad j = 5, 10, \ldots, 40 \tag{22}$$

where the power spectrum p_j of a signal $\dot{u}_r(t)|_j$ at each measurement point j was calculated as:

$$p_j = \int_{f_c - 2f_m}^{f_c + 2f_m} \left| \hat{\dot{u}}_r(f)|_j \right|^2 df \approx \sum_{i=k}^{i=l} \hat{\dot{u}}_r(f_i) \hat{\dot{u}}_r^*(f_i)|_j, \quad i = 1, 2, \ldots, n, \quad j = 1, 5, 10, \ldots, 40 \tag{23}$$

based on its discrete Fourier transform $\hat{\dot{u}}_r(f_i)|_j$, where n is the total number of samples and where $\hat{\dot{u}}_r^*(f_i)|_j$ is a complex conjugate of $\hat{\dot{u}}_r(f_i)|_j$. The values of indexes k and l were determined according to a very simple relationship as $k = \min\{i : f_i \geq f_c - 2f_m\}$ and $l = \max\{i : f_i \leq f_c + 2f_m\}$.

It can be noted that the greatest values of the damping coefficient ζ_j are obtained for the carrier frequency f_c of 20 kHz reaching 24.6 dB at the 25th unit cell, while its averaged value is 13.3 dB. In the case of the carrier frequency f_c of 10 kHz the damping coefficient ζ_j reaches its maximum of 10.9 dB at the 40th unit cell, while its averaged value is 2.4 dB. Finally, in the case of the carrier frequency f_c of 30 kHz the damping coefficient ζ_j reaches its maximum of 18.3 dB at the 30th unit cell, while its averaged value is 10.6 dB.

7. Conclusions

The results presented in this paper can be divided into three separate categories. The first category of results concerns modelling techniques employed by the authors in order to investigate dynamic properties as well as dynamic responses of a three-dimensional periodic beam. The second category of results concern the optimisation procedure used by the authors to adjust parameters of their numerical models to achieve predefined dynamic properties of the beam in terms of the position and width of a common frequency band gap. The final category of results concerns those of experimental measurements by one-dimensional laser Doppler scanning vibrometry.

Based on the authors' investigations described in this paper the following general conclusions can be drawn:

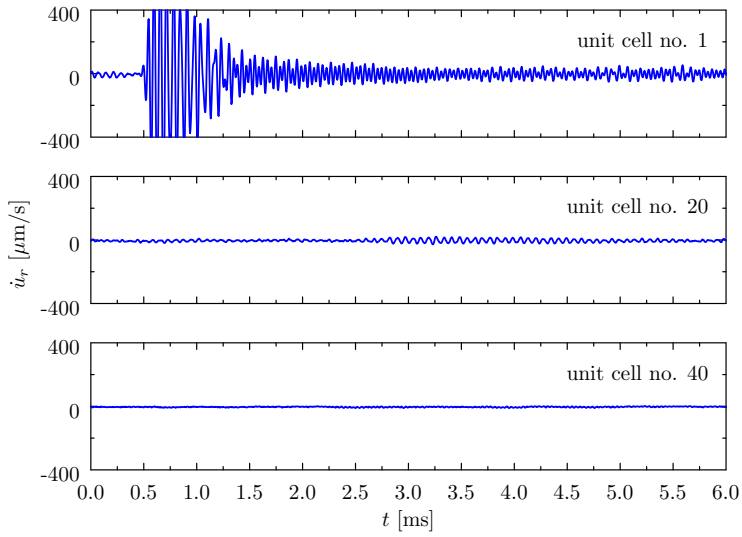

Figure 22: Wave propagation patterns of a periodic beam measured experimentally by the use of 1-D LDSV, for the radial component $\dot{u}_r$ of beam vibrations, for the discrete values of $r_i = \{7.6, 37.2, 27.8, 37.2, 7.7, 7.6\}$ mm. Results obtained for the carrier frequency f_c of the excitation signal equal to 20 kHz within the common frequency band gap Δf_c.

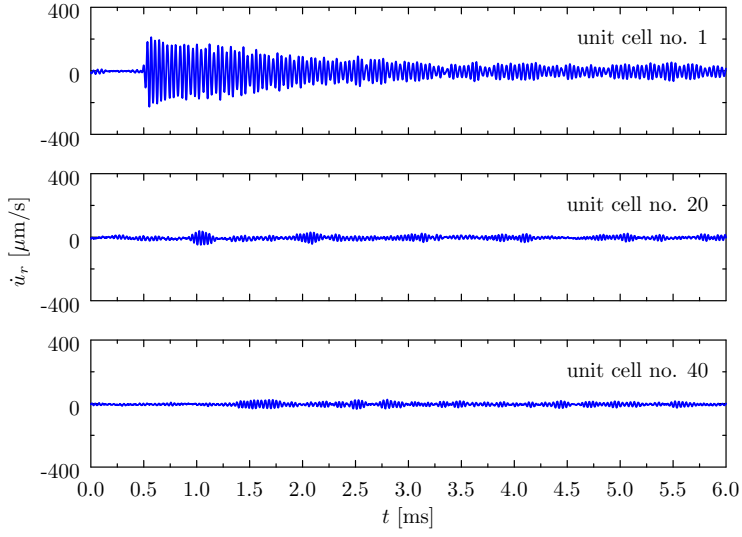

Figure 23: Wave propagation patterns of a periodic beam measured experimentally by the use of 1-D LDSV, for the radial component $\dot{u}_r$ of beam vibrations, for the discrete values of $r_i = \{7.6, 37.2, 27.8, 37.2, 7.7, 7.6\}$ mm. Results obtained for the carrier frequency f_c of the excitation signal equal to 30 kHz outside the common frequency band gap Δf_c.

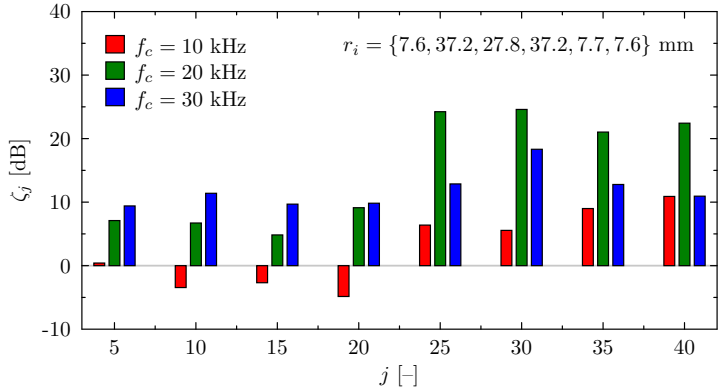

Figure 24: Variation of a vibroacoustic damping coefficient ζ_j of a periodic beam, based on results of experimental measurements by the use of 1-D LDSV, for the radial component $\dot{u}_r$ of beam vibrations, for the discrete values of $r_i = \{7.6, 37.2, 27.8, 37.2, 7.7, 7.6\}$ mm. Results obtained for the carrier frequencies f_c of the excitation signal equal to 10 kHz, 20 kHz and 30 kHz.

- A new, isoparametric, 6-node spectral finite element (SFE), based on Chebyshev node distribution has been developed by the authors. This SFE has been designed in order to investigate dynamic behaviour of axisymmetrical beam-like structural elements of varying geometry. Thanks to a smooth and continuous variation of its geometry the element is especially well suited to study the dynamic behaviour of periodic structures. It should be noted that geometrical discontinuities between adjacent finite elements (FEs) can have a great impact on the correctness and applicability of numerical models in the case of their application [31] to the study of periodic structures.

- Due to significant changes in SFEs geometry, expressed by the element radius, extended forms of the displacement fields for particular types of beam vibrations have been used, i.e. 6-mode theory of longitudinal behaviour, 8-mode of flexural behaviour and 3-mode of torsional behaviour. As a consequence of this, a very good agreement between numerical results obtained by the use of the current SFE and known analytical solutions have been achieved in the cases of longitudinal, flexural and torsional behaviour of the beam, in a very wide range of frequencies up to 5 MHz·mm.

- The optimisation procedure employed by the authors allowed them to adjust geometrical parameters of particular SFEs within a single cell defining a periodic beam. Thanks to this the width and the position of a resulting common frequency band gap can be arbitrary selected in the cases of longitudinal, flexural and torsional vibrations, within the natural frequency spectrum of the periodic beam under investigation.

- The correctness and the applicability of the formulated SFE as well as the optimisation procedure have been successfully verified by the use of the classical finite element method (FEM). For that purpose a numerical model has been prepared by the authors using the Autodesk Simulation Mechanical software, which consisted 1.2 million 4-node tetrahedral FEs (770,000 DOF) in comparison to 200 SFE of 6-node elements (17,017 DOF in total, for all types of beam vibrations). A numerical model proposed by the authors has been therefore less than one forty-fifth the size of the model used by the classical FEM, making the current approach not only computationally faster and more robust, but also very well suited for various optimisation algorithms.

- The results of numerical computations obtained by the authors using the current SFE have also been successfully verified by the results of experimental measurements using of one-dimensional laser Doppler scanning vibrometry (1-D LDSV). Moreover, the result of experimental measurements have stayed in very good agreement with the results of the optimisation procedure and have confirmed the applicability of periodic structures as vibroacoustic isolators or filters.

- The approach presented by the authors in the present paper together with the optimisation procedure can be potentially applied to other similar problems related to the application of periodic structures such as vibroacoustic isolators or filters in the cases when only particular types of vibrations must be eliminated. They indicate the capabilities offered by numerical modelling and optimisation methods that can be successfully employed in order to design periodic structures of predefined dynamic properties, i.e. the widths and the positions of frequency band gaps in their vibration spectra.

8. Acknowledgements

The authors of this work would like to gratefully acknowledge the support for their research provided by the National Science Centre via project UMO-2012/07/B/ST8/03741 *Wave propagation in periodic structures*. All results presented in this paper have been obtained by the use of the software available at the Academic Computer Centre in Gdansk in the frame of a computational project.

References

[1] K. M. Ho, C. T. Chan, C. M. Soukoulis, Existence of a photonic gap in periodic dielectric structures, Physical Review Letters 65 (1990) 3152–3155.
[2] M. S. Kushwaha, M. S. Halevi, L. Dobrzynski, B. Djafarirouhani, Acoustic band-structure of periodic elastic composites, Physical Review Letters 71 (1993) 2022–2025.
[3] K. M. Ho, C. T. Chan, C. M. Soukoulis, R. Biswas, M. Sigalas, Photonic band-gaps in 3-dimensions – New layer-by-layer periodic structures, Solid State Communications 89 (1994) 413–416.
[4] J. V. Sánchez-Pérez, D. Caballero, R. Mártinez-Sala, C. Rubio, J. Sanchez-Dehesa, F. Meseguer, J. Llinares, F. Gálvez, Sound attenuation by two-dimensional array or rigid cylinders, Physical Review Letters 80 (1998) 5325–5328.
[5] S. Yang, J. H. Page, Z. Y. Liu, M. L. Cowan, C. T. Chan, P. Sheng, Focusing of sound in a 3d phononic crystal, Physical Review Letters 93 (2004) 024301:1–4.
[6] D. L. Yu, Y. Z. Liu, H. G. Zhao, G. Wang, J. Qiu, Flexural vibration band gaps in Euler-Bernoulli beams with locally resonant structures with two degrees of freedom, Physical Review B 73 (2006) 064301:1–5.
[7] Y. Xiao, J. H. Wen, G. Wang, X. S. Wen, Theoretical and experimental study of locally resonant and Bragg band gaps in flexural beams carrying periodic arrays of beam-like resonators, Journal of Vibration and Acoustic –Transaction of the ASME 135 (2013) 041006:1–17.
[8] D. Duhamel, B. R. Mace, M. J. Brennan, Finite element analysis of the vibrations of waveguides and periodic structures, Journal of Sound and Vibration 294 (2006) 205–220.
[9] X. N. Liu, G. K. Hu, C. T. Sun, G. L. Huang, Wave propagation characterization and design of two-dimensional elastic chiral metacomposite, Journal of Sound and Vibration 330 (2011) 2536–2533.
[10] J. C. Hsu, Local resonances-induced low-frequency band gaps in two-dimensional phononic crystal slabs with periodic stepped resonators, Journal of Physics D: Applied physics 44 (2011) 055401:1–9.
[11] A. Żak, M. Krawczuk, M. Palacz, Ł. Doliński, W. Waszkowiak, High frequency dynamics of an isotropic Timoshenko periodic beam by the use of time-domain spectral finite element method, Journal of Sound and Vibration 409 (2017) 318–335.
[12] S. H. Lee, C. M. Park, Y. M. Seo, Z. G. Wang, C. K. Kim, Composite acoustic medium with simultaneously negative density and modulus, Physical Review Letters 104 (2010) 054301:1–4.
[13] F. R. M. de Espinosa, E. Jimenez, M. Torres, Ultrasonic band gap in a periodic two-dimensional composite,, Physical Review Letters 80 (1998) 1208–1211.
[14] B. Bonello, C. Charles, F. Ganot, Lamb waves in plates covered by a two-dimensional phononic film, Applied Physics Letters 90 (2007) 021909:1–3.
[15] L. Brullouin, Wave propagation in periodic structures: Electric filters and crystal lattices, McGraw-Hill Book Company, Inc., New York, 1946.
[16] S. Halkjær, O. Sigmund, J. S. Jensen, Maximizing band gaps in plate structures, Structural and Multidisciplinary Optimization 32 (2006) 263–275.
[17] N. W. Ashcroft, N. D. Mermin, Solid State Physics, Holt, Rinehart and Winston, New York, 1976.
[18] W. Ostachowicz, P. Kudela, M. Krawczuk, A. Żak, Guided Waves in Structures for SHM. The Time-domain Spectral Element Method, John Wiley & Sons Ltd., Singapore, 2012.
[19] O. C. Zienkiewicz, The Finite Element Method, McGraw-Hill Book Company, London, 1989.
[20] J. P. Boyd, Chebyshev and Fourier Spectral Methods, Dover Publications, Inc., New York, 2000.
[21] J. D. Achenbach, Wave Propagation in Elastic Solids, North-Holland Publishing Company, Amsterdam, 1973.
[22] J. L. Rose, Ultrasonic Waves in Solid Media, Cambridge University Press, Cambridge, 1999.
[23] A. Żak, M. Krawczuk, Assessment of rod behaviour theories used in spectral finite element modelling, Journal of Sound and Vibration 329 (2010) 2099–2113.
[24] A. Żak, M. Krawczuk, Assessment of flexural beam behaviour theories used for dynamics and wave propagation problems, Journal of Sound and Vibration 331 (2012) 5715–5731.

[25] J. F. Doyle, Wave Propagation in Structures, Springer-Verlag, Inc., New York, 1997.
[26] http://www.wolfram.com/.
[27] http://www.mathworks.com/.
[28] J. Kennedy, R. C. Eberhart, Y. Shi, Swarm Intelligence, Academic Press, San Diego, 2001.
[29] S. Koziel, Computationally efficient multi-fidelity multi-grid design optimization of microwave structures, Applied Computational Electromagnetics Society Journal 25 (2010) 578–2010.
[30] A. Żak, M. Krawczuk, A higher order transversely deformable shell-type spectral finite element for dynamic analysis of isotropic structures, Finite Elements in Analysis and Design 141 (2018) 17–29.
[31] A. Żak, M. Krawczuk, M. Palacz, Periodic properties of 1-D FE discrete models in high-frequency dynamics, Mathematical Problems in Engineering Article ID 9651430 (2015) 1–15.